Iterative image restoration using nonstationary priors

Esteban Vera,[1,*] Miguel Vega,[2] Rafael Molina,[3] and Aggelos K. Katsaggelos[4]

[1]Department of Electrical and Computer Engineering, University of Arizona, Tucson, Arizona 85721, USA

[2]Departamento de Lenguajes y Sistemas Informáticos, Universidad de Granada, Granada 18071, Spain

[3]Departamento de Ciencias de la Computación e I.A., Universidad de Granada, Granada 18071, Spain

[4]Department of Electrical Engineering and Computer Science, Northwestern University, Evanston, Illinois 60208, USA

*Corresponding author: estebanvera@u.arizona.edu

Received 16 November 2012; revised 11 February 2013; accepted 11 February 2013;
posted 12 February 2013 (Doc. ID 179373); published 29 March 2013

In this paper, we propose an algorithm for image restoration based on fusing nonstationary edge-preserving priors. We develop a Bayesian modeling followed by an evidence approximation inference approach for deriving the analytic foundations of the proposed restoration method. Through a series of approximations, the final implementation of the proposed image restoration algorithm is iterative and takes advantage of the Fourier domain. Simulation results over a variety of blurred and noisy standard test images indicate that the presented method comfortably surpasses the current state-of-the-art image restoration for compactly supported degradations. We finally present experimental results by digitally refocusing images captured with controlled defocus, successfully confirming the ability of the proposed restoration algorithm in recovering extra features and rich details, while still preserving edges.

OCIS codes: 100.3020, 100.1830, 100.3190, 110.3010.

1. Introduction

Imaging systems are often affected by several degradation sources, leading to blurry and noisy images that are not necessarily a faithful representation of the desired targets. Therefore, and regardless of the employed modality, image restoration is a critical task for recovering useful imagery for a variety of applications, for example, remote sensing, surveillance, medical diagnosis, and astronomy [1]. For instance, optical imaging systems, such as digital photographic or scientific cameras, are not exempt from producing degraded imagery, despite the availability of modern CCD or CMOS imaging detectors with improved resolution, extended dynamic range, and increased quantum efficiency. In digital images, blurring-like degradations can be produced by optical aberrations or misalignments (optical blur), turbulence (atmospheric blur), or motion due to the nonzero aperture time (motion blur) [2]. In addition, noise can appear due to quantum and thermal effects, detector nonuniformity, aliasing, electronics readout, and quantization.

Unfortunately, the restoration of blurred and noisy images is an ill-posed inverse problem [3]. Henceforth, it has to be typically solved by constrained optimization yielding iterative regularization methods [4]. Nonetheless, regularized image restoration has to solve two main problems: the choice of the regularization function and the regularization parameter, or Lagrange multiplier. The use of Bayesian methods for image restoration has emerged as an elegant way of describing the regularization term by means of *a prior* distribution, with the additional ability of allowing estimation of both the regularization and noise variance weights. Although it has been successfully applied to smoothness promoting priors [5,6], Bayesian modeling imposes restrictions on the choice of the prior function, since some arbitrary priors may lead to intractable inference problems. Nevertheless, the variational Bayes approximation [7] has allowed

1559-128X/13/10D102-09$15.00/0

successful use of nonstationary sparsity promoting priors within the Bayesian framework, such as total variation (TV) in [8], Gaussian scale mixtures in [9], and the product of student-t experts in [10,11].

In this paper we propose a new approach to the combination of nonstationary edge-preserving image priors. The novel approach follows the spirit of the prior model based on the product experts first proposed in [12], but this time without the need for modifying the observation model, or the need for using or setting any weighting parameters. The inference procedure is now based on the evidence approximation, or type-II maximum likelihood, continuing the same avenue introduced in [5] for stationary Bayesian image restoration. However, in this particular case, the resulting iterative parameter estimation update algorithm is computationally intractable. Consequently, we propose a series of empirical approximations. In this way, the resulting iterative restoration algorithm is not only effective, but also efficient, as it can also be implemented in the Fourier domain.

We provide simulations for testing the proposed restoration algorithm and compare its performance with state-of-the-art Bayesian restoration algorithms. We also present results from a digital refocusing experiment for images captured with different out-of-focus levels. Quantitative and qualitative evaluation of both simulated and real experimental results confirms the extended capabilities of the proposed restoration method in recovering more appealing images with enhanced details.

The paper is organized as follows. Section 2 presents the Bayes modeling and introduces the proposed new prior for the image restoration problem. In Section 3, the inference procedure for image and parameter estimation is derived. Empirical approximations are explained in Section 4, leading to an efficient implementation. Sections 5 and 6 present the results obtained for the simulations and the digital refocusing experiment. Finally, conclusions are drawn in Section 7.

2. Bayesian Modeling

A. Observation Model

A typical linear model for image degradation considers that the observed image $\mathbf{y}$, in lexicographical order, is the result of the convolution of the original and unknown image $\mathbf{x}$ with a blurring kernel operator $\mathbf{H}$ plus some additive noise $\mathbf{n}$; that is,

$$\mathbf{y} = \mathbf{H}\mathbf{x} + \mathbf{n}. \tag{1}$$

Assuming the noise component $\mathbf{n}$ follows a Gaussian distribution, the probability density function of the observation model is expressed as

$$p(\mathbf{y}|\mathbf{x},\beta) \propto \beta^{N/2} \exp\left\{-\frac{\beta}{2}\|\mathbf{y}-\mathbf{H}\mathbf{x}\|^2\right\}, \tag{2}$$

with β the inverse of the noise variance, and N the total number of pixels in the image.

B. Prior Model

Inspired by the results obtained when combining more than one single prior, as in the Markov random fields (MRF) experts used for image denoising in [13], or the sparse prior approach used for image deconvolution in [14] and the references therein, we continue down the path of the product of experts used in [12], but now following a different inference procedure without approximating the covariance matrix for the prior prematurely.

Therefore, as an image prior we define a zero-mean multivariate Gaussian distribution that combines the constraints given by a set of L filters $\mathbf{C}_i$ as follows:

$$p(\mathbf{x}|\mathbf{a}_1,\ldots,\mathbf{a}_L) \propto \left|\sum_{i=1}^{L}\mathbf{C}_i^t\mathbf{A}_i\mathbf{C}_i\right|^{1/2} \exp\left\{-\frac{1}{2}\sum_{i=1}^{L}\|\mathbf{A}_i^{1/2}\mathbf{C}_i\mathbf{x}\|^2\right\}, \tag{3}$$

where $\mathbf{A}_i$ is an $N\times N$ diagonal matrix containing the hyperparameters α_i^j associated with the inverse variance (precision) of the response of each corresponding filter operator $\mathbf{C}_i$ for any given pixel j. Thus, $\mathbf{A}_i = \mathrm{DIAG}(\mathbf{a}_i)$, and $\mathbf{a}_i = [a_i^1, a_i^2, \ldots, a_i^N]^t$.

The advantage of using the proposed prior modeling is twofold. First, we avoid the election of any specific sparsity promoting shape for the prior distribution, as is done in [10]. Second, by choosing a multivariate Gaussian distribution, we are able to seek a tractable inference mechanism.

3. Bayesian Inference

The joint probability density function is written as

$$\begin{aligned} p(\mathbf{y},\mathbf{x},\beta,\mathbf{a}_1,\ldots,\mathbf{a}_L) &\propto p(\mathbf{y}|\mathbf{x},\beta)p(\mathbf{x}|\mathbf{a}_1,\ldots,\mathbf{a}_L) \\ &\propto \left|\sum_{i=1}^{L}\mathbf{C}_i^t\mathbf{A}_i\mathbf{C}_i\right|^{1/2} \beta^{N/2} \\ &\quad\times \exp\left\{-\frac{1}{2}\sum_{i=1}^{L}\|\mathbf{A}_i^{1/2}\mathbf{C}_i\mathbf{x}\|^2\right\} \\ &\quad\times \exp\left\{-\frac{\beta}{2}\|\mathbf{y}-\mathbf{H}\mathbf{x}\|^2\right\}. \end{aligned} \tag{4}$$

We choose to perform the inference for the desired hyperparameters based on the evidence analysis—also known as empirical Bayes or type-II maximum likelihood—previously used in image restoration with stationary priors in [5,6]. Then, by marginalizing over $\mathbf{x}$ we have that

$$p(\mathbf{y}|\beta,\mathbf{a}_1,\ldots,\mathbf{a}_L) \propto \int_{\mathbf{x}} p(\mathbf{y},\mathbf{x},\beta,\mathbf{a}_1,\ldots,\mathbf{a}_L)\mathrm{d}\mathbf{x}, \tag{5}$$

and thus

$$\ln p(\mathbf{y}|\beta,\mathbf{a}_1,\ldots,\mathbf{a}_L,) = \frac{1}{2}\ln\left|\sum_{i=1}^{L}\mathbf{C}_i^t\mathbf{A}_i\mathbf{C}_i\right| + \frac{N}{2}\ln\beta - \frac{1}{2}\sum_{i=1}^{L}\|\mathbf{A}_i^{1/2}\mathbf{C}_i\bar{\mathbf{x}}\|^2 - \frac{\beta}{2}\|\mathbf{y}-\mathbf{H}\bar{\mathbf{x}}\|^2 - \frac{1}{2}\ln\left|\sum_{i=1}^{L}\mathbf{C}_i^t\mathbf{A}_i\mathbf{C}_i + \beta\mathbf{H}^t\mathbf{H}\right|. \tag{6}$$

Now, by taking the derivative with respect to the hyperparameter α_i^j, we have

$$\frac{\delta\ln p(\mathbf{y}|\beta,\mathbf{a}_1,\ldots,\mathbf{a}_L)}{\delta\alpha_i^j} = \frac{1}{2}\left(\text{trace}\left[\left(\sum_{i=1}^{L}\mathbf{C}_i^t\mathbf{A}_i\mathbf{C}_i\right)^{-1}\mathbf{C}_i^t\mathbf{J}^{jj}\mathbf{C}_i\right] - \bar{\mathbf{x}}^t\mathbf{C}_i^t\mathbf{J}^{jj}\mathbf{C}_i\bar{\mathbf{x}} - \text{trace}\left[\left(\sum_{i=1}^{L}\mathbf{C}_i^t\mathbf{A}_i\mathbf{C}_i+\beta\mathbf{H}^t\mathbf{H}\right)^{-1}\mathbf{C}_i^t\mathbf{J}^{jj}\mathbf{C}_i\right]\right), \tag{7}$$

where $\bar{\mathbf{x}}$ is the maximum *a posteriori* estimate for the unknown image obtained by solving

$$\bar{\mathbf{x}} = \left(\sum_{i=1}^{L}\mathbf{C}_i^t\mathbf{A}_i\mathbf{C}_i + \beta\mathbf{H}^t\mathbf{H}\right)^{-1}\mathbf{H}^t\mathbf{y}, \tag{8}$$

and $\mathbf{J}^{jj}$ is a special selection matrix that is zero everywhere except for the entry (jj). Note that Eq. (8) can be iteratively solved using a conjugate gradient (CG) minimization algorithm.

Now, by setting the derivative in Eq. (7) equal to zero, and defining $\Sigma_P = \sum_{i=1}^{L}\mathbf{C}_i^t\mathbf{A}_i\mathbf{C}_i$, $\Sigma_T = \sum_{i=1}^{L}\mathbf{C}_i^t\mathbf{A}_i\mathbf{C}_i + \beta\mathbf{H}^t\mathbf{H}$, and $\nu_i = \mathbf{C}_i\bar{\mathbf{x}}$, Eq. (7) can be rewritten as

$$\text{trace}[\Sigma_P^{-1}\mathbf{C}_i^t\mathbf{J}^{jj}\mathbf{C}_i] = (\nu_i^j)^2 + \text{trace}\left[\Sigma_T^{-1}\mathbf{C}_i^t\mathbf{J}^{jj}\mathbf{C}_i\right]. \tag{9}$$

Then, following a similar approach for updating the hyperparameters to the one in [5], we derived the following iterative formula for any of the hyperparameters α_i^j at iteration $(k+1)$:

$$\alpha_i^{j(k+1)} = \frac{\text{trace}[\Sigma_P^{(k)-1}\mathbf{C}_i^t\mathbf{J}^{jj}\mathbf{C}_i]}{(\nu_i^{j(k)})^2 + \text{trace}[\Sigma_T^{(k)-1}\mathbf{C}_i^t\mathbf{J}^{jj}\mathbf{C}_i]}\alpha_i^{j(k)}, \tag{10}$$

where $\bar{\mathbf{x}}^{(k)}$ (needed to calculate $\nu_i^{(k)}$) is computed at each iteration (k) using Eq. (8) with the required hyperparameter matrices $\mathbf{A}_i^{(k)}$ obtained from the previous iteration of Eq. (10), along with the corresponding covariances $\Sigma_P^{(k)-1}$ and $\Sigma_T^{(k)-1}$.

4. Implementation

Unfortunately, the parameter-update formula in Eq. (10) is not tractable as is, mostly due to the computation of the inverse of the covariance matrices, Σ_P^{-1} and Σ_T^{-1}, since they are extremely large. Therefore, we start tackling this problem by applying the Jacobi diagonal approximation to the covariance matrices, which leads to the straightforward inversion

$$\Sigma_P^{(k)-1} \approx \text{DIAG}(\zeta_P^{(k)}), \qquad \Sigma_T^{(k)-1} \approx \text{DIAG}(\zeta_T^{(k)}). \tag{11}$$

Here, $\zeta_P^{(k)}$ and $\zeta_T^{(k)}$ are $N\times 1$ vectors with components $\zeta_P^{l(k)} = 1/\sigma_P^{l(k)}$ and $\zeta_T^{l(k)} = 1/\sigma_T^{l(k)}$, respectively, for $l = 1,\ldots,N$. Moreover, $\sigma_P^{(k)} = \sum_{i=1}^{L}\mathbf{D}_i\mathbf{a}_i^{(k)}$ and $\sigma_T^{(k)} = \sigma_P^{(k)} + \beta h^2$, where $\mathbf{D}_i$ are $N\times N$ filter matrices with elements $D_i^j = (C_i^j)^2$, for $i = 1,\ldots,L$. Also, the constant h is obtained as the sum of the squares of the point spread function (PSF) kernel elements, which in the case of the boxcar (uniform) PSF is equivalent to the value of any of the nonzero kernel coefficients.

Using a similar approach, we have

$$\mathbf{C}_i^t\mathbf{J}^{jj}\mathbf{C}_i \approx \mathbf{S}_i^{jj}, \tag{12}$$

where $\mathbf{S}_i^{jj} = \text{DIAG}(\gamma_i^j)$. Here $\gamma_i^j = \mathbf{F}_i\mathbf{j}^j$ are $N\times 1$ vectors for $i = 1,\ldots,L$, while $\mathbf{j}^j$ is an $N\times 1$ vector that is zero everywhere except at the position j. Similarly to the matrices D_i, $\mathbf{F}_i$ are also $N\times N$ filter matrices with elements $F_i^j = (C_i^j)^2$. Thus, we finally have that

$$\text{trace}[\Sigma_P^{-1}\mathbf{C}_i^t\mathbf{J}^{jj}\mathbf{C}_i] \approx \text{trace}[\Sigma_P^{-1}\mathbf{S}_i^{jj}]. \tag{13}$$

Finally, by applying both approximations provided by Eqs. (11) and (13) over Eq. (10), in addition to stacking into vector form for the different $\alpha_i^{j(k+1)}$ components, a new update rule can be obtained for each of the hyperparameter diagonal matrices as follows:

$$\mathbf{A}_i^{(k+1)} \approx \left[\text{DIAG}\left(\mu_i^{(k)} + \mathbf{F}_i\Sigma_T^{(k)-1}\vec{\mathbf{1}}\right)\right]^{-1}\text{DIAG}\left(\mathbf{F}_i\Sigma_P^{(k)-1}\mathbf{a}_i^{(k)}\right), \tag{14}$$

where $\mu_i^{(k)} = (\nu_i^{(k)})^2$, and, as explained before, each $\mathbf{F}_i$ is related to each respective filter $\mathbf{C}_i$, for $j = 1,\ldots,N$.

Through experimentation we have found that better and more stable results are finally obtained when the filters $\mathbf{F}_i$ are replaced by a unique filter $\mathbf{F}$, whose corresponding kernel $\mathbf{f}$ is given by

$$\mathbf{f} = \begin{bmatrix} 0 & 1 & 0 \\ 1 & 1 & 1 \\ 0 & 1 & 0 \end{bmatrix}. \tag{15}$$

Due to the fact that Eq. (14) deals with diagonal matrices, it can be efficiently implemented in the

Fourier domain. In this way, we have the advantage of obtaining all the diagonal elements of the inverse of each covariance matrix at once, leading to compute the different hyperparameters α_i^j in parallel, for $i = 1, \ldots, L$.

5. Simulation Results

We performed several experiments for restoring images with simulated blur and noise, using Matlab implementations of state-of-the-art restoration algorithms, and different versions of the herein-proposed restoration method. We implemented our algorithm in Eq. (14) using two options: NF2 that uses only the first-order difference filters, such as

$$\mathbf{c}_1 = \frac{1}{\sqrt{2}}[1\ -1], \qquad \mathbf{c}_2 = \frac{1}{\sqrt{2}}[1\ -1]^t; \tag{16}$$

and NF4 that also adds the diagonal filters $\mathbf{c}_3$ and $\mathbf{c}_4$ defined as follows:

$$\mathbf{c}_3 = \frac{1}{\sqrt{2}}\begin{bmatrix} 1 & 0 \\ 0 & -1 \end{bmatrix}, \qquad \mathbf{c}_4 = \frac{1}{\sqrt{2}}\begin{bmatrix} 0 & 1 \\ -1 & 0 \end{bmatrix}. \tag{17}$$

We compared the restoration performance of both versions against implementations of the Bayesian total variation (BTV) approach [8], and the product of student-t priors (BST) [10]. We tested the restoration algorithms in a set of four standard images: cameraman (CAM, 256×256), Lena (LEN, 256×256), Shepp–Logan phantom (PHA, 256×256) and Barbara (BAR, 512×512. The images were degraded by applying one of the following PSFs: a 9×9 uniform blur, or a Gaussian blur with variance $\sigma^2 = 9$. Also, Gaussian noise was added for achieving an equivalent blurred signal-to-noise ratio (BSNR) of 40, 30, or 20 dB.

For all experiments, every algorithm received as inputs the blurred image, the blurring PSF kernel, and the noise variance $\sigma^2 = 1/\beta$. In addition, the stopping criterion for the iterative update of the hyperparameters was that the condition $\|\mathbf{x}^{(k)} - \mathbf{x}^{(k-1)}\| < 10^{-3}$ was met. Also, the CG iterative process for estimating the restored image [Eq. (8)] was terminated using a threshold of 10^{-4} or a maximum of 1000 iterations. Finally, the performance for each restoration was measured in terms of the improvement in signal-to-noise ratio (ISNR), which is defined as $20\log_{10}(\|\mathbf{x} - \mathbf{y}\|/\|\mathbf{x} - \hat{\mathbf{x}}\|)$, with $\hat{\mathbf{x}}$ the restored image. The average results obtained for the restoration performance for five noise realizations are summarized in Table 1.

Analyzing the results in Table 1, we observe that in the particular case of the boxcar uniform kernel, the proposed algorithm in both of its versions presents an overall superior ISNR for the majority of the tested images and noise levels, except for the phantom image at higher noise situations, where BST performs better. This seems reasonable since BST enforces sparsity in a stronger way, which makes it more suitable for piecewise smooth images.

Nevertheless, a different outcome is obtained from Table 1 when restoring for the Gaussian PSF. Even though both NF2 and NF4 perform better for the cameraman image, they only surpass BTV when restoring a highly corrupted Lena with strong noise. A similar situation can be observed for the phantom image, where BST wins in low to mid noise levels, while NF4 is the best with more noise, counterintuitively to what was previously noticed for the uniform kernel restoration. Last, both versions of the proposed algorithm reach a competitive quality for Barbara compared to BTV for all noise levels.

Although NF2 performs great, or at least provides competitive results when compared to BTV or BST, the addition of two extra prior filters in the case of NF4 allows us to often significatively boost the performance. Note that for images degraded by the uniform PSF, NF4 outperforms BTV, and often BST, for more than 10%, leading to a considerable improvement of more than 1 dB in ISNR for both the cameraman and Lena images for all noise levels. Restoration samples for the 40 dB degraded cameraman can be seen in Fig. 1, where the recovered images with both versions of the proposed algorithm (NF2 and NF4)

Table 1. Comparative Restoration Performance Results in Terms of the ISNR (dB)

		Uniform Kernel (9×9)				Gaussian Kernel ($\sigma^2 = 9$)			
BSNR	Method	CAM	LEN	PHA	BAR	CAM	LEN	PHA	BAR
40 dB	BTV	8.60	8.51	17.74	3.22	3.49	**4.85**	7.87	**1.61**
	BST	8.80	8.13	19.02	3.16	3.25	4.34	**10.34**	1.36
	NF2	9.34	9.13	20.03	**3.74**	3.56	3.87	5.39	1.54
	NF4	**9.75**	**9.63**	**23.05**	3.65	**3.71**	4.03	8.06	1.52
30 dB	BTV	5.08	5.89	11.00	1.71	2.73	**3.96**	5.29	**1.27**
	BST	5.89	5.50	**12.51**	1.61	2.69	3.08	**7.97**	1.04
	NF2	6.38	6.40	10.44	**2.01**	3.03	3.37	5.71	1.18
	NF4	**6.61**	**6.86**	12.14	1.93	**3.17**	3.49	6.43	1.20
20 dB	BTV	2.42	3.59	5.52	1.15	1.81	2.84	2.79	**1.14**
	BST	3.18	2.65	**8.25**	0.73	2.03	1.93	5.16	0.79
	NF2	**3.85**	4.22	6.83	**1.35**	2.36	**3.18**	5.10	1.11
	NF4	3.70	**4.45**	7.84	1.33	**2.41**	3.11	**5.70**	1.09

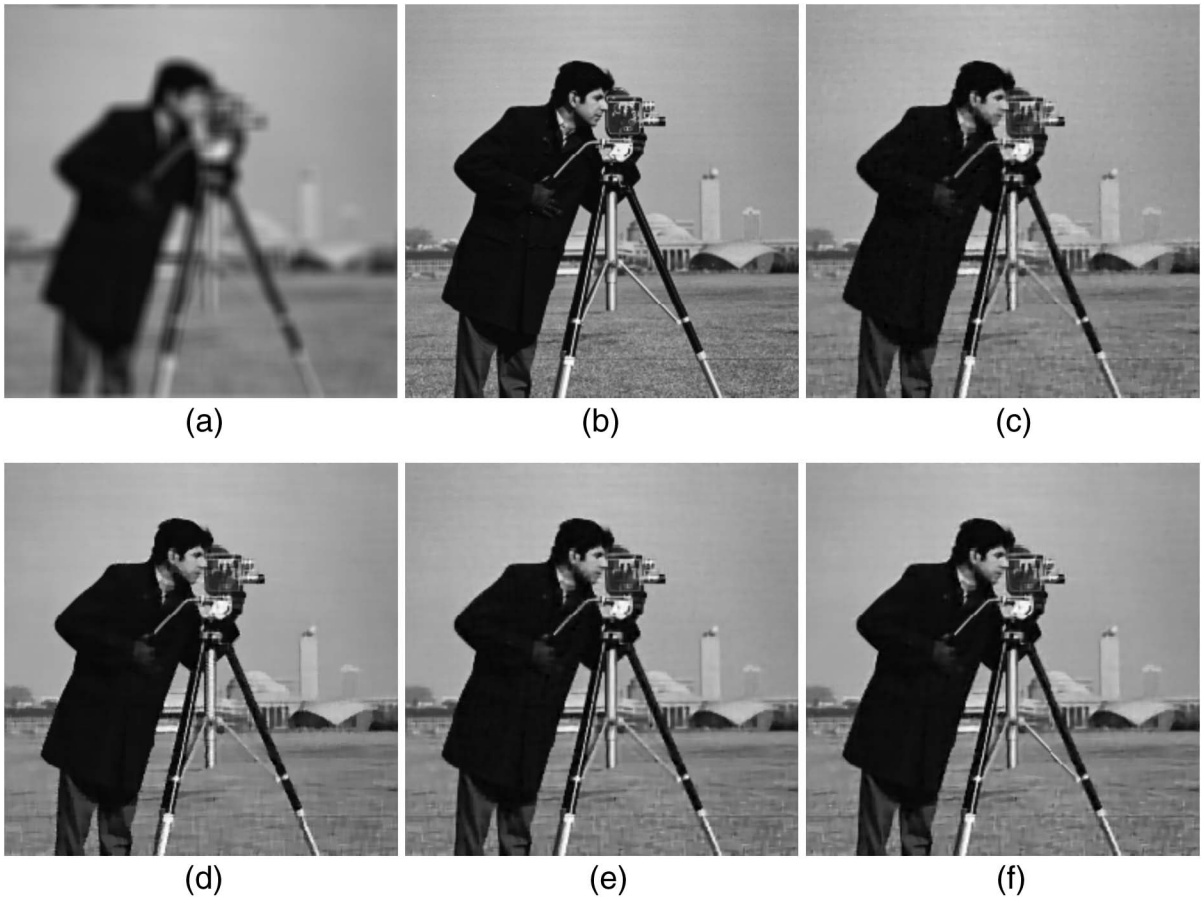

Fig. 1. Restoration results for cameraman corrupted with a 9×9 uniform kernel and 40 dB BSNR. (a) Degraded; (b) original; (c) BTV, ISNR = 8.60 dB; (d) BST, ISNR = 8.80 dB; (e) NF2, ISNR = 9.34 dB; and (f) NF4, ISNR = 9.75 dB.

seem to have more details than with BTV or BST, while still preserving edges and diminishing noise.

By examining Fig. 1 we notice that the results by NF2 and NF4 are comparable in terms of visual quality, which is confirmed by the reported ISNR. A naked-eye evaluation allows us to perceive that the restored images using NF2 or NF4 are smoother and less piecewise-like than the BTV and BST versions. Now, when closely inspecting the zoomed-in portions in Fig. 2, we can see that in the regular areas, such as the skin, the smooth degrade and shadowing effects due to illumination are better recovered. Nevertheless, even though some edges are better defined—see the tripod pivot and handler—we are able to notice the appearance of some artifacts near some of the edges. Although not displayed here, we can report that those artifacts are mostly reduced when using more priors, such as in the case of NF4 compared to NF2. Furthermore, and as seen in Fig. 2, at lower noise levels these artifacts tend to be perceived only at very magnified inspections, while the overall perceived quality of the proposed restoration method is very good in terms of recovered details.

6. Experimental Results

We designed an experiment for systematically defocusing a target picture, while also retrieving the respective PSF from an illuminated optical fiber. For that, we mounted in a standard optical table a QImaging RETIGA EXi Monochrome 12 bit cooled CCD camera attached to a Computar H6Z0812 8–48 mm F1.2 *C*-mount zoom lens. We placed the desired target pictures at a distance of 1 m from the main lens. We set the lens by fixing the f-stop at 4, and the focal distance at 30 mm. The idea was to allow a proper focusing at the chosen distance, with enough depth of field in order to assure the nearest spatially invariant optical transfer function (OTF) at the widest area in the field of view (FOV). We balanced the lighting conditions and integration time for compensating for the small aperture. In addition, we mounted at the same target distance one end of an optical fiber right at the center of the FOV, illuminated at the other end by a Thorlabs OSL 1-EC halogen lamp fiber illuminator. In this way, we are able to interchange between the target image and the end of the optical fiber, and the procedure for the experiment is explained as follows. First, by turning off all the lights except the fiber illuminator, we focus the fiber light source onto the detector, changing the integration time for not saturating it until we see a PSF with the smallest possible support, hopefully within 1 pixel and its closest neighbors. Second, we place the target picture in place, turn on the ambient lights, and take a picture, adjusting the integration time for

Fig. 2. Zoomed-in restoration results for cameraman corrupted with a 9×9 uniform kernel and 40 dB BSNR. (a) Original; (b) BTV, ISNR = 9.34 dB; and (c) NF4, ISNR = 9.75 dB.

maximum SNR. This will become the focused, or ground-truth, image. Finally we change the focus and repeat the first two steps without concern for the PSF size, but recording it for all the different levels of defocus as wanted, as well as alternately capturing the corresponding defocused target images.

From all the experiments made using the aforementioned procedure for several defocus levels and different target images, we applied all the implemented algorithms as described in the previous section. However, now we utilized the procedure formerly proposed in [15] for confidently estimating the noise precision parameter β, using it as an input to all the deconvolution methods. In addition, we retrieve from the pictures of the illuminated fiber the associated PSF for each target image, normalizing it for being handed to the algorithms as the effective blurring kernel that degraded the images to be restored.

The first experiment consisted of using a picture of several image thumbnails of natural images. Each image was finally captured by a small area of the CCD detector, leading to a resolution of 100×80 pixels each. Also, the illumination and integration time were adjusted for not saturating any of the images. From the images located near the center of the FOV, where we can assure that the estimated PSF is actually the most likely to have caused the degradation, we present some sample results in Figs. 3 and 4.

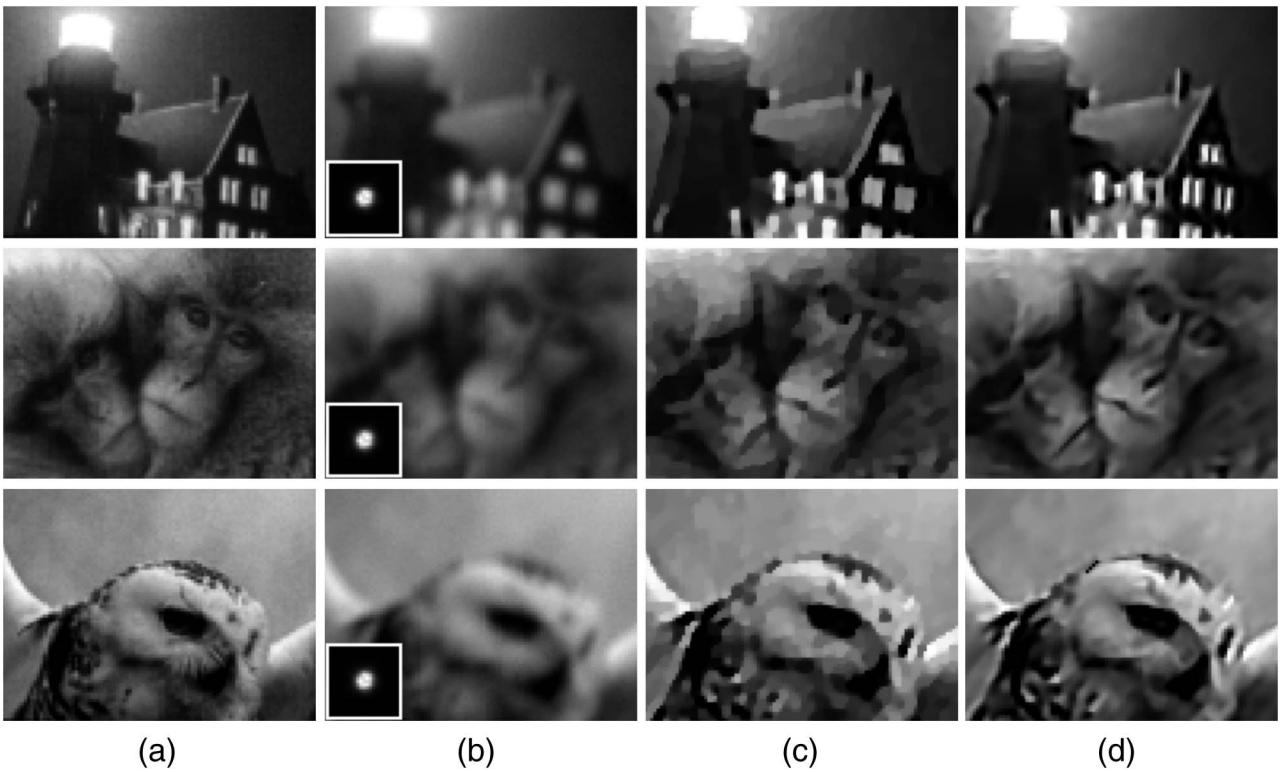

Fig. 3. Digital refocusing image samples using a medium defocus. (a) Focused image, (b) defocused image (inset: measured PSF), (c) BTV restoration, and (d) NF4 restoration.

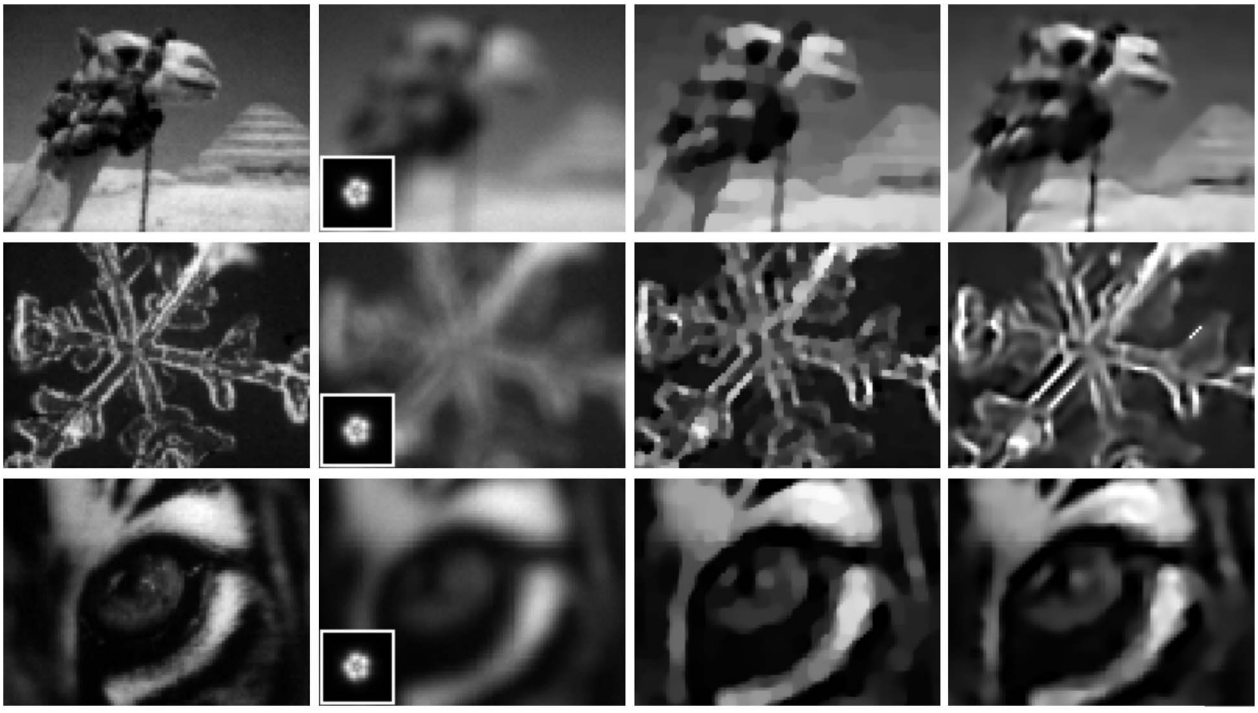

Fig. 4. Digital refocusing image samples using a strong defocus. (a) Focused image, (b) defocused image (inset: measured PSF), (c) BTV restoration, and (d) NF4 restoration.

Figure 3 presents the restoration results from defocused images with medium size defocus, whose PSF support has a diameter of around 6 pixels [see inset in the blurred images of Fig. 3(b)], where we can notice a clear difference in terms of restoration quality between BTV in Fig. 3(c) and NF4 in Fig. 3(d). For instance, inspecting the first row, we can check that NF4 was able to recover details from the windows of the house that are lost in BTV. Another feature, already visualized in the simulations, was that NF4 is able to recover smooth transitions of nontextured areas, such as the roof and the light source from the house image, the mouth of the mandrills, and the background from the owl image. In addition, NF4 generates restorations that have less piecewise appearance—which often resemble some quantization effects—than those restored with BTV, producing more appealing images. Nonetheless, even though NF4 produces more pleasant restorations, some of the anticipated artifacts that arose in the simulations presented in Section 5 may be noticed, specially in the owl image (third row).

Similarly, images restored from a larger defocus are shown in Fig. 4, where the retrieved PSF has nearly 12 pixels of diameter, which produces severely defocused images as displayed in Fig. 4(b). Again, NF4 seems to reconstruct images with enhanced details in comparison to BTV. An analysis similar to that previously performed for Fig. 3 also holds. Although the support of the PSF is larger, which usually makes the deconvolution task more difficult, the camel image restored by NF4 has plenty of details, such as the mouth, nose, and accessories of the camel, that have been lost when using BTV. The snowflake shown in the second row also makes clear the ability of NF4 in recovering finer details and well-defined edges. The eye of the tiger in the last row is a good example of the smooth transitions allowed by NF4 restorations, while BTV still produces piecewise results, which is a typical feature in pure sparsity promoting priors, such as BST as well.

Finally in Fig. 5, we present the results of the last experiment that uses as a target a single larger image of a printed black and white photography (400×210) pixels. Fig. 5(a) shows the ground truth focused image and its respective PSF (inset). Note the cross-like shape of the PSF, concentrating most of the energy in the center pixel. Figures 5(b)–5(d) show images obtained for progressive increases in defocus, where the support of the associated PSFs (see insets) varies from values near 5, 7, and 11 pixels, respectively. Also note that the larger PSF no longer follows a circular shape, but it has a shape that resembles the aperture iris of the lens. The restored images obtained by using the proposed NF4 are displayed in Figs. 5(e)–5(g). At a first sight, from an appropriate distance of the screen or a printed version (1 m away may suffice), all the restored images seem, at least, to be in focus. On the other hand, and as is expected, when closely inspecting the results we can verify that more details can be recovered when restoring less degraded images. In particular, Fig. 5(e) shows a very good restoration, recovering the majority of the most significative details such

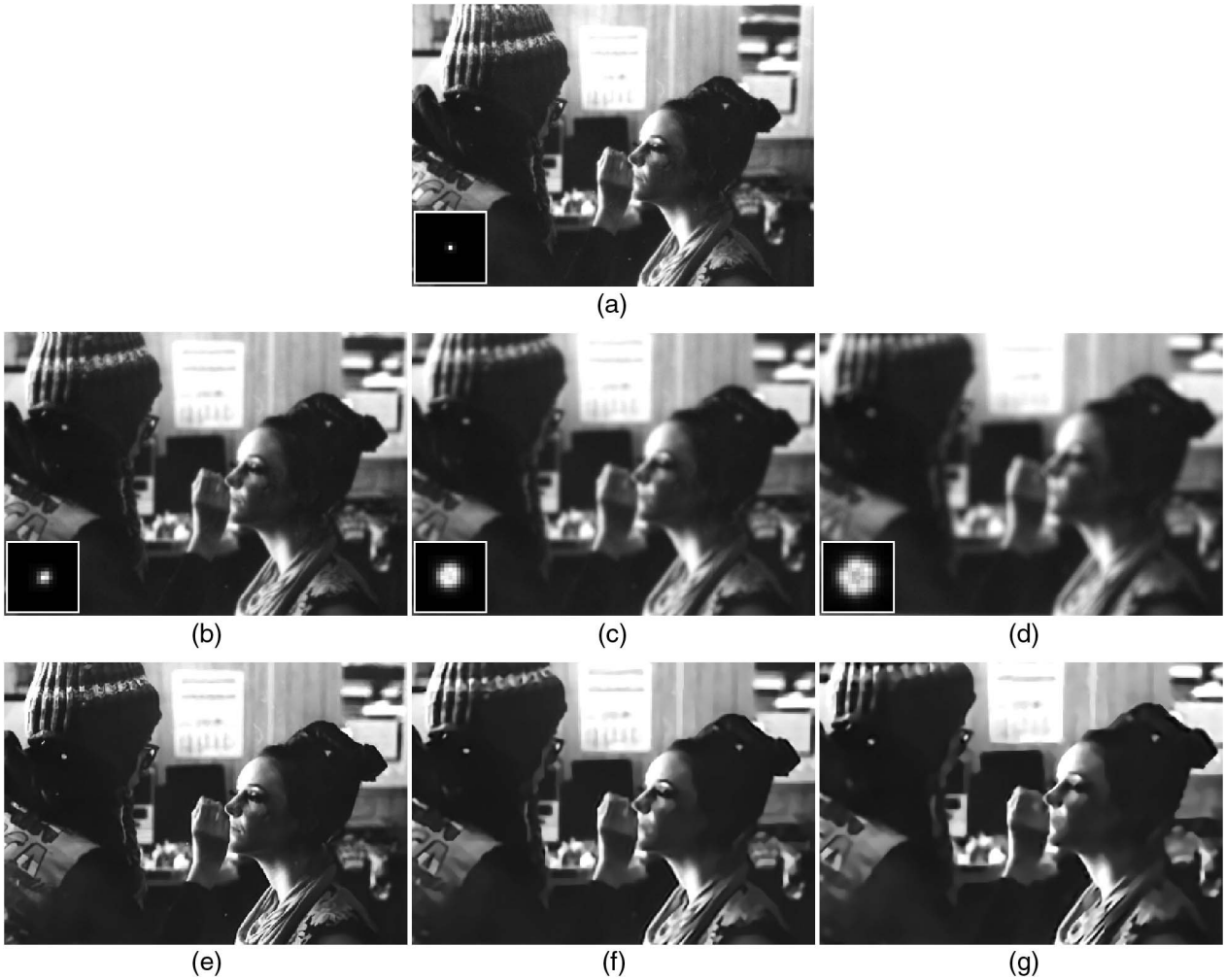

Fig. 5. Digital refocusing experiment. (a) Focused image (inset: 4× measured PSF), (b) moderate defocus image (inset: 4× measured PSF), (c) medium defocus image (inset: 4× measured PSF), (d) strong defocus image (inset: 4× measured PSF), (e) restored image (b) using NF4, (f) restored image (c) using NF4, (g) restored image (d) using NF4.

as the blouse wrinkles and flowers, the hat textures, while wiping out only the finest details of the make up on the face, when compared to the ground truth image. Despite performing the restoration of a larger blur see Fig. 5(f) NF4 is still able to recover the most noticeable blouse features, and also most of the shadows and diffuse reflections on the face. Last, from Fig. 5(g) we can still appreciate most of the important features of the face, marked by well-defined edges such as the nose and eyebrow contour, but most of the details have been smeared, which would most likely happen as well when using any other edge preserving deconvolution algorithm, such as BTV, although not as smoothly as with NF4.

7. Conclusion

In this paper, we proposed a new algorithm for image restoration based on combining nonstationary edge-preserving priors. We developed a Bayesian modeling followed by an evidence analysis inference approach for deriving the initial parameter-update algorithm. From there, the iterative algorithm was empirically approximated tackling its computational difficulties, mostly related to the inversion of large and ill-posed covariance matrices, and also allowing a fast and efficient implementation through the Fourier domain. When comparing the restoration results of the proposed method with some of the latest state-of-the-art image restoration algorithms (BTV [8] and BST [10]) on a set of standard test images with simulated blurring and noise, we concluded that despite some exceptions, the proposed algorithm outperformed the current available methods in terms of ISNR and visual quality, especially when restoring natural images from blur kernels with compact support. The reported ISNR values, in particular for the uniform PSF, indicate that the proposed algorithm, in all its implemented versions, surpassed by more than 10% the other methods, reaching a gap of more than 1 dB for the classic cameraman and Lena test images for all noise levels. Nevertheless, for the Gaussian PSF case the results were not the most prominent ones, but they were competitive.

We finally tested the algorithms with a digital refocusing experiment for a variety of defocused natural images. As expected, the proposed NF4 clearly outperformed BTV in visual quality, producing pleasing images that remarkably presented a wider recovery of details, while allowing realistic smooth transitions instead of piecewise solutions typically found when employing TV and sparse regularizers. In summary, we proposed a restoration algorithm that comfortably surpassed the state-of-the-art image restoration in terms of ISNR for the majority of the standard tested cases, especially for compactly supported degradations. The proposed method also proved to be suitable for restoring defocused images with a clear enhancement in the perceivable visual quality. The latter makes it especially interesting for restoring the boxcar pixel PSF found in superresolution reconstruction applications, and for coded aperture image recovery problems. Further work may include the development of new and improved ways of approximating the parameter estimation stage of the algorithm, while also extending its usage to blind deconvolution and computational photography applications.

This work was supported in part by the Ministerio de Ciencia e Innovación under contract TIN2010-15137. Esteban Vera is grateful to Dr. Sergio Torres and Dr. Carlos Saavedra at the Center for Optics and Photonics (CEFOP), University of Concepcion, Chile, for providing partial financial support through grant PFB08024.

References

1. M. Banham and A. Katsaggelos, "Digital image restoration," IEEE Signal Process. Mag. **14**(2), 24–41 (1997).
2. H. C. Andrews and B. R. Hunt, *Digital Image Restoration* (Prentice-Hall, 1977).
3. M. Bertero and P. Boccacci, *Introduction to Inverse Problems in Imaging* (Taylor & Francis, 1998).
4. A. Katsaggelos, S. Babacan, and C.-J. Tsai, "Iterative image restoration," in *The Essential Guide to Image Processing*, A. Bovik, ed. (Elsevier, 2009), Chap. 15.
5. R. Molina, "On the hierarchical Bayesian approach to image restoration: applications to astronomical images," IEEE Trans. Pattern Anal. Mach. Intell. **16**, 1122–1128 (1994).
6. R. Molina, A. Katsaggelos, and J. Mateos, "Bayesian and regularization methods for hyperparameter estimation in image restoration," IEEE Trans. Image Process. **8**, 231–246 (1999).
7. D. Tzikas, A. Likas, and N. Galatsanos, "The variational approximation for Bayesian inference," IEEE Signal Process. Mag. **25**(6), 131–146 (2008).
8. S. Babacan, R. Molina, and A. Katsaggelos, "Parameter estimation in tv image restoration using variational distribution approximation," IEEE Trans. Image Process. **17**, 326–339 (2008).
9. R. Fergus, B. Singh, A. Hertzmann, S. T. Roweis, and W. T. Freeman, "Removing camera shake from a single photograph," ACM Trans. Graph. **25**, 787–794 (2006).
10. G. Chantas, N. Galatsanos, A. Likas, and M. Saunders, "Variational Bayesian image restoration based on a product of t-distributions image prior," IEEE Trans. Image Process. **17**, 1795–1805 (2008).
11. G. Chantas, N. Galatsanos, R. Molina, and A. Katsaggelos, "Variational Bayesian image restoration with a product of spatially weighted total variation image priors," IEEE Trans. Image Process. **19**, 351–362 (2010).
12. G. Chantas, N. Galatsanos, and A. Likas, "Bayesian restoration using a new nonstationary edge-preserving image prior," IEEE Trans. Image Process. **15**, 2987–2997 (2006).
13. S. Roth and M. J. Black, "Fields of experts," Int. J. Comput. Vis. **82**, 205–229 (2009).
14. S. Babacan, R. Molina, M. Do, and A. Katsaggelos, "Blind deconvolution with general sparse image priors," in *Proceedings of European Conference on Computer Vision (ECCV)* (Springer, 2012), pp. 341–355.
15. R. Molina, J. Mateos, and A. Katsaggelos, "Blind deconvolution using a variational approach to parameter, image, and blur estimation," IEEE Trans. Image Process. **15**, 3715–3727 (2006).